ChemComm

COMMUNICATION

View Article Online
View Journal | View Issue

Cite this: *Chem. Commun.*, 2025, **61**, 8011

Received 16th April 2025,
Accepted 28th April 2025

DOI: 10.1039/d5cc02137e

rsc.li/chemcomm

Foreign cation-promoted active species formation enables efficient electrochemical glycerol valorization†

Hojeong Lee,[a] Jihoo Cha,[a] Sun Gwan Cha,[b] Tae-Hoon Kong,[a] Namgyoo Park,[a] Seontaek Kwon,[a] Hyung Ju Kim[c] and Youngkook Kwon*[ab]

The foreign cation substitution approach to Ni–Co spinel oxide promotes the active NiOOH species formation, resulting in remarkable electrochemical glycerol oxidation activity and selectivity for formate production. The generated NiOOH improves both the indirect GOR and the coadsorption capacity of OH* and glycerol, which is crucial to the potential-dependent GOR mechanism.

The electrochemical glycerol oxidation reaction (GOR) powered by renewable electricity offers a sustainable route to boost the utility of excess glycerol from the biodiesel industry, by converting it into high value-added products.[1] In particular, formic acid (or formate in neutral and alkaline media) is a promising target product because of its importance as a chemical intermediate in various industrial processes,[2] as well as its potential as a viable hydrogen carrier with a high volumetric hydrogen capacity (53 g H_2 per L) and minimal toxicity.[3]

Co-based spinel oxides are widely used in numerous electrocatalytic reactions, including the GOR, because of their exceptional stability in oxidative environments. However, Co_3O_4 itself exhibits poor GOR activity and low formate selectivity due to its limited electrical conductivity and a d-band center close to the Fermi level.[4] In contrast, Ni-based catalysts are known for their high selectivity for formate production, attributed to their favorable C–C bond cleavage ability.[5] Therefore, incorporation of Ni into the Co_3O_4 structure (*e.g.*, $Ni_1Co_2O_4$) enables selective GOR for formate production.[4] For Ni sites of Ni–Co spinel oxide to function as active sites for the GOR, Ni oxyhydroxide (NiOOH) species must form through surface reconstruction.[1] However, due to the electrochemical stability of pristine Ni–Co spinel oxide,[6] large overpotentials are required to form active NiOOH species. Since increasing the overpotential accelerates both the competing OER and overoxidation of GOR products, it is crucial to promote the activation of the Ni sites in Ni–Co spinel oxide to enhance formate electrosynthesis from glycerol.

In this work, we present a strategy to enhance the GOR performance for formate production through foreign cation (Fe) substitution, which lowers the electrochemical reconstruction potential of Ni–Co spinel oxide and facilitates the formation of active NiOOH species. Using nickel foam (NF) as a substrate, we synthesized Co spinel oxide (Co_3O_4/NF, denoted as CO/NF), Ni–Co spinel oxide ($Ni_1Co_2O_4$/NF, denoted as NCO/NF), and Fe substituted-NCO/NF (denoted as Fe–NCO/NF). The Fe–NCO/NF catalyst demonstrated high GOR activity with significant formate selectivity, resulting in formate production rates that were ~2.59 and ~5.00 times higher compared to NCO/NF and CO/NF, respectively. *In situ* Raman measurements and *operando* electrochemical impedance spectroscopy (EIS) analyses reveal that Fe substitution promotes the formation of NiOOH, which participates directly in the indirect GOR mechanism (non-electrochemical reaction).[7] In addition, control experiments using electrolytes with varying OH^- and glycerol concentrations demonstrate that NiOOH enhances the potential-dependent GOR.

The synthesis of the catalysts follows a two step process, including hydrothermal and calcination (Tables S1 and S2, ESI†). Field emission-scanning electron microscopy (FE-SEM) images clearly show that all the catalysts exhibit a similar nanoneedle morphology (Fig. 1a and Fig. S1a and S2, ESI†), indicating that the incorporation of foreign cations does not significantly alter the structure of Co-based spinel oxide. Similarly, transmission electron microscopy (TEM) images for Fe–NCO/NF and NCO/NF show that they exhibit nearly identical nanorod-like morphologies (Fig. 1b and Fig. S1b, ESI†). The high-resolution TEM (HR-TEM) image of Fe–NCO/NF represents distinct lattice spacings of 0.244 nm and 0.469 nm, corresponding to the (311) and (111) facets of $Ni_1Co_2O_4$, respectively (Fig. 1c and Note S1, ESI†),[4]

[a] *School of Energy and Chemical Engineering, Ulsan National Institute of Science and Technology (UNIST), Ulsan 44919, Republic of Korea. E-mail: ykwon@unist.ac.kr*
[b] *Graduate School of Carbon Neutrality, UNIST, Ulsan 44919, Republic of Korea*
[c] *Advanced Materials Division, Korea Research Institute of Chemical Technology (KRICT), 141 Gajeong-ro, Yuseong-gu, Daejeon, 34114, Republic of Korea*

† Electronic supplementary information (ESI) available. See DOI: https://doi.org/10.1039/d5cc02137e

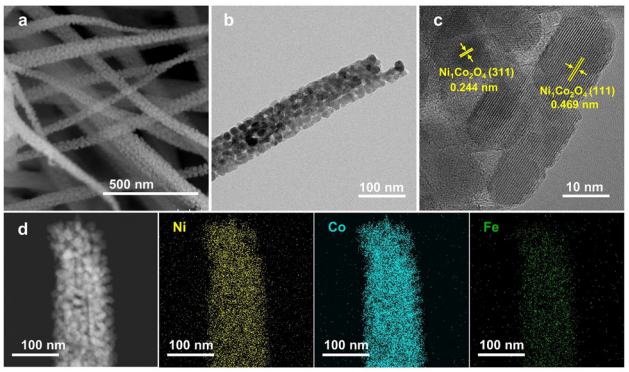

Fig. 1 (a) SEM, (b) TEM, and (c) HR-TEM images of Fe–NCO/NF. (d) TEM images and corresponding elemental mapping.

which can be attributed to the similar cation radii of Fe, Co, and Ni.[8] The energy dispersive spectrometer (EDS) mapping images of Fe–NCO/NF and NCO/NF show a uniform distribution of all elements (Ni, Co, Fe, and O) within the nanorod morphology (Fig. 1d and Fig. S1c, d and Fig. S3, ESI†).[4]

The high-resolution XRD (HR-XRD) spectra (Fig. 2a) of CO/NF and NCO/NF are well matched to Co_3O_4 (JCPDS# 01-080-1542) and $Ni_1Co_2O_4$ (JCPDS# 01-073-1702), respectively. The spinel structure of $Ni_1Co_2O_4$ is maintained in Fe–NCO/NF after Fe substitution, consistent with the HR-TEM results (Note S1, ESI†). Raman spectroscopy analyses were conducted on CO/NF, NCO/NF, and Fe–NCO/NF to examine the substitution behavior of Ni and Fe within the Co spinel oxide structure (Fig. 2b). The Co-based spinel oxide exhibits F^1_{2g}, E_g, F^2_{2g}, F^3_{2g}, and A_{1g} vibrational modes within the Raman shift range of 150 to 900 cm^{-1} (Note S1, ESI†).[9,10] The substitution of Ni and Fe induces a shift in the A_{1g} peak position of the Co-based spinel oxide, while the F^1_{2g} peak remains unchanged. This indicates that Ni and Fe are exclusively substituted into the octahedral coordination site in NCO/NF and Fe–NCO/NF. The comparison of XRD and Raman analyses confirms the successful substitution of Fe for Co and Ni at the octahedral coordination sites of Fe–NCO/NF.

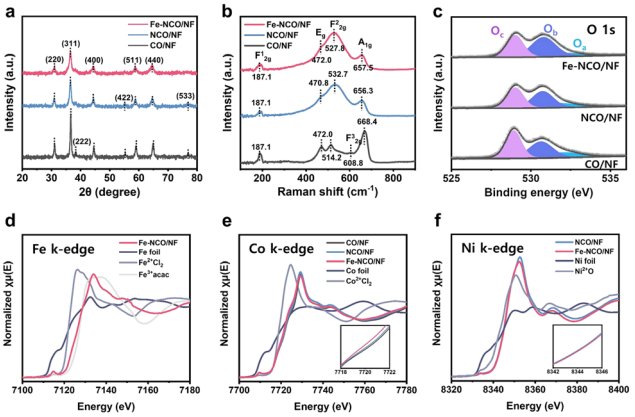

Fig. 2 Structure and chemical characterization of the CO/NF, NCO/NF, and Fe-NCO/NF catalysts. (a) XRD pattern and (b) Raman spectra of the catalysts. (c) XPS spectra of O 1s. XANES spectra of (d) Fe K-edge, (e) Co K-edge, and (f) Ni K-edge.

The surface chemical states of the catalysts were analyzed by X-ray photoelectron spectroscopy (XPS). The comparison of the O 1s spectra of the catalysts demonstrated that the introduction of Fe increases the amount of oxygen vacancies on the Co-based spinel oxide (Fig. 2c and Fig. S4a and Note S1, ESI†). The Co 2p spectra display two peaks at 779.5 eV (Co $2p_{3/2}$) and 794.48 eV (Co $2p_{1/2}$), representing Co^{2+} and Co^{3+} oxidation states, along with corresponding satellite peaks (Fig. S5–S7, ESI†).[11] The Co^{2+}/Co^{3+} ratio of Fe–NCO/NF (1.67) is higher than that of NCO/NF (1.23) and CO/NF (0.94), indicating the substitution of Co^{3+} by Ni and Fe in the octahedral coordination sites (Fig. S4b, ESI†). The Ni 2p spectra show two peaks at 855.08 eV (Ni $2p_{3/2}$) and 872.58 eV (Ni $2p_{1/2}$), along with their respective satellite peaks. Fe substitution in Fe–NCO/NF slightly increases the Ni valence state compared to NCO/NF (Fig. S4b, S6 and S7, ESI†).

Fig. 2d–f shows the X-ray absorption near-edge structure (XANES) analysis of Fe, Co, and Ni K-edge to investigate the local electronic structure of the catalysts. The Fe K-edge XANES spectra confirm the presence of Fe in Fe–NCO/NF, consistent with the TEM-EDS and Fe 2p XPS results (Fig. 1d, 2d and Fig. S7a, ESI†). The Co K-edge XANES spectra for CO/NF, NCO/NF, and Fe–NCO/NF show an increased adsorption edge compared to the $CoCl_2$ reference, suggesting that the Co in all three catalysts is in a higher valence state than Co^{2+}. In addition, comparison of the three catalysts reveals that the incorporation of Fe and Ni into the Co-based spinel oxide results in a decrease in the Co valence state, which aligns with the XPS Co 2p spectra (Fig. 2e and Fig. S4b, ESI†). The Ni K-edge XANES spectra for NCO/NF and Fe–NCO/NF display elevated adsorption edges relative to the NiO reference, confirming that Ni in both catalysts exhibits a higher valence state than Ni^{2+} (Fig. 2f).

The electrochemical performances of CO/NF, NCO/NF, and Fe–NCO/NF were evaluated to investigate the Fe substitution effects on activity and selectivity, by using 1 M KOH for the OER condition and 1 M KOH with 0.1 M glycerol for the GOR condition. To compare the ability of the catalysts to form oxyhydroxide species, cyclic voltammograms (CV) were obtained under OER conditions (Fig. 3a). Due to the introduction of Ni, CO/NF and the other two catalysts exhibit different CV behaviors.[12] For NCO/NF and Fe–NCO/NF, the initial anodic peak corresponds to the generation of oxyhydroxide by catalyst oxidation.[8] A first anodic peak of Fe–NCO/NF required a lower potential compared to NCO/NF, indicating that the pre-oxidation of the catalyst can be improved by Fe substitution, which consequently promotes the formation of active oxyhydroxide species.[8]

The comparison of the linear sweep voltammogram (LSV) curves under GOR conditions (Fig. 3b) suggests that the GOR activity of the Fe–NCO/NF catalyst (1.198 V_{RHE}@10 mA cm^{-2}, 1.308 V_{RHE}@100 mA cm^{-2}) is superior to those of NCO/NF and CO/NF, indicating that the enhanced oxyhydroxide formation by Fe substitution has a beneficial effect on the GOR. Moreover, the enhanced GOR activity of Fe–NCO/NF was further evidenced by its lower Tafel slope and charge transfer resistance (R_{CT}) values in comparison with NCO/NF and CO/NF (Fig. 3c and Fig. S8, ESI†). Consequently, Fe–NCO/NF showcases excellent GOR activity, competitive with currently reported non-precious

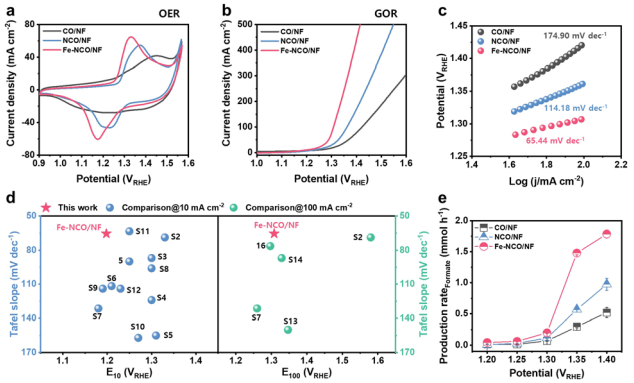

Fig. 3 Electrocatalytic performance of CO/NF, NCO/NF, and Fe–NCO/NF catalysts. (a) CV curves of the catalysts in 1 M KOH electrolyte. (b) LSV curves and (c) Tafel slopes of the catalysts in 1 M KOH with 0.1 M glycerol electrolyte. (d) Comparison of GOR activity of Fe–NCO/NF with state-of-the-art non-precious metal-based catalysts (the details of (d) are provided in Table S3, ESI†). (e) Comparison of the formate production rate of the catalysts.

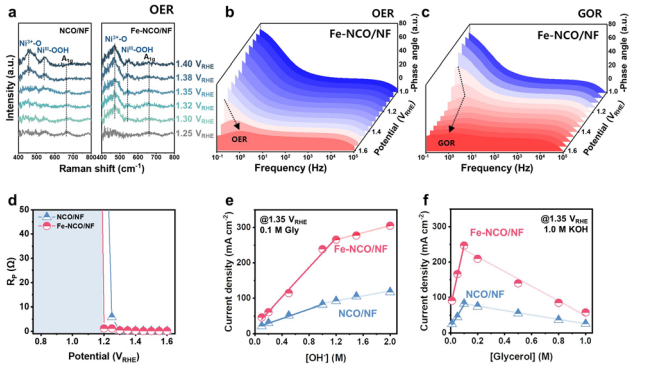

Fig. 4 Investigations of the Fe-substitution effect on the GOR mechanism. (a) *In situ* Raman spectroscopy measurements of the catalysts in 1 M KOH electrolyte. (b) and (c) Bode phase plots of the *operando* EIS analyses of Fe–NCO/NF in (b) OER and (c) GOR conditions. (d) The fitting results of polarization resistance of the catalysts as a function of potential. The dependence of GOR current density on the concentration of (e) KOH and (f) glycerol at 1.35 V_{RHE}.

metal-based electrocatalysts regarding Tafel slope and the applied potential necessary to achieve 10 and 100 mA cm^{-2} (Fig. 3d and Table S3, ESI†). We note that all catalysts exhibited enhanced activity under GOR conditions compared to the OER, suggesting that GOR could serve as a viable alternative anode reaction to the OER (Fig. S9, ESI†). Additionally, the comparison of the electrical double layer capacitance (EDLC, C_{dl}) values shows that the incorporation of heteroelements (Ni, Fe) slightly increased the number of active sites in the catalyst, but not the primary factor influencing the GOR activity (Fig. S10, ESI†).

The product distribution of the GOR was evaluated using chronoamperometry (CA) measurements within overoxidation-free potential ranges from 1.20 V_{RHE} to 1.40 V_{RHE} for 60 min, with the corresponding products quantified through high-performance liquid chromatography (HPLC) (Fig. S11, ESI†). For all catalysts, increasing the applied potential from 1.20 V_{RHE} to 1.40 V_{RHE} resulted in a decrease in the $FE_{Glycolate}$, whereas the $FE_{Formate}$ increased, indicating that the C–C cleavage step is facilitated at elevated overpotentials (Fig. S12, ESI†). Interestingly, NCO/NF and Fe–NCO/NF demonstrated almost identical $FE_{formate}$ in the low potential region ($\leq$1.25 V_{RHE}), with slight deviations observed above 1.30 V_{RHE}. This suggests that the oxyhydroxide formation ability influences the C–C cleavage step of the GOR (Fig. S12a–d, ESI†). Moreover, Fe–NCO/NF showed higher formate production rates (1.785 $\pm$ 0.062 mmol h^{-1}@1.40 V_{RHE}) and enhanced glycerol conversion (66.2 $\pm$ 4.41%@1.40 V_{RHE}) due to its significant activity towards the GOR and superior C–C cleavage ability, outperforming its counterparts (Fig. 3e and Fig. S12e, ESI†). Performance comparisons employing commercial Pt/C and controlled samples with an increased Fe quantity emphasized the superior formate electrosynthesis ability of Fe–NCO/NF and demonstrated that Fe does not significantly impact GOR performance (Supporting Note S2, S3 and Fig. S13–S17, ESI†). Furthermore, various stability tests and post-mortem analyses underscored the remarkable catalytic stability of Fe–NCO/NFs (Supporting Note S4 and Fig. S18–S24, ESI†).

To gain insight into the Fe substitution effect on the formation of oxyhydroxide species, we performed *in situ* Raman spectroscopy measurements in 1 M KOH electrolyte at different potentials (Fig. 4a). As the potential increased, two new peaks emerged, corresponding to Ni^{3+}–O ($\sim$470 cm^{-1}) and Ni^{III}–OOH ($\sim$552 cm^{-1}), suggesting the formation of active NiOOH species.[13] Notably, Fe–NCO/NF exhibits a reduced electrochemical reconstruction potential (1.30 V_{RHE}) for the NiOOH species compared to NCO/NF (1.38 V_{RHE}), indicating that Fe substitution facilitates the formation of active species in Ni–Co spinel oxide, consistent with the CV curve results.

To determine whether the catalysts follow the indirect GOR mechanism,[14] we conducted additional control experiments. After applying enough potential for NiOOH formation (1.40 V_{RHE}) under OER conditions, temporarily disconnecting the potential and quickly adding glycerol eliminated the NiOOH-related peak from the *in situ* Raman spectra (Fig. S25, ESI†). Moreover, *in situ* Raman spectra acquired under GOR conditions showed that the detection of NiOOH-related peaks required a higher potential in the presence of nucleophilic molecules (Fig. S25, ESI†). These results suggest that Fe–NCO/NF and NCO/NF follow an indirect GOR mechanism and that a foreign cation-promoted NiOOH formation facilitates these non-electrochemical GORs of Ni–Co spinel oxide catalysts.

To examine the impact of Fe substitution on the electrode/electrolyte interface, we conducted *operando* EIS analyses on Fe–NCO/NF and NCO/NF (Fig. 4b, c and Fig. S26, S27, ESI†).[15] The comparison of the polarization resistance (R_P) values as a function of potential (Fig. 4d) shows that the R_P values of Fe–NCO/NF were significantly lowered at 1.20 V_{RHE}, indicating that Fe–NCO/NF has a reduced electrochemical reconstruction potential compared to NCO/NF (starts at 1.25 V_{RHE}). In addition, both catalysts exhibited a sharp decrease in R_{CT} value at 1.20 V_{RHE}, with Fe–NCO/NF showing a reduced value at the same potential (Fig. S27e, ESI†). Therefore, the *operando* EIS analyses suggest that the foreign cation enhances both the

NiOOH formation ability and the activity of the potential-dependent GOR on Ni–Co spinel oxide catalysts. A more detailed discussion is provided in Note S5 (ESI†).

Given that effective coadsorption of OH* and glycerol on the catalyst surface is critical for the potential-dependent GOR mechanism, we examined the impact of NiOOH on the coadsorption of both species. *In situ* Raman spectroscopy measurements under GOR conditions revealed that at 1.35 V_{RHE}, only Fe–NCO/NF generates sufficient amounts of NiOOH for detection (Fig. S25, ESI†), making 1.35 V_{RHE} an optimal potential for evaluating the effect of NiOOH on the potential-dependent GOR mechanism. To assess the OH* adsorption capacity of NiOOH, we acquired LSV curves using electrolytes with different OH^- concentrations, while keeping the glycerol concentration at 0.1 M, and compared the current density values at 1.35 V_{RHE} (Fig. S28, ESI†). Fig. 4e shows that Fe–NCO/NF demonstrated a broader potential range of first linear relationship compared to NCO/NF. The second linear relationship is attributable to the hindrance of glycerol adsorption as the catalytic active site becomes predominantly occupied by OH*.[16] These finding indicate that Fe–NCO/NF (with NiOOH) exhibits enhanced OH* adsorption capacity compared to NCO/NF (without NiOOH) at 1.35 V_{RHE}. Then, we performed a similar experiment using electrolytes with differing glycerol concentrations while maintaining a constant KOH concentration (1.0 M) (Fig. S29, ESI†). Both catalysts showed a linear relationship with a positive slope at low glycerol concentrations, followed by a negative slope when the glycerol concentrations exceeded 0.1 M (Fig. 4f). Fe–NCO/NF showed a sharper slope in both linear regions compared to NCO/NF, indicating a greater glycerol adsorption capacity.[16] These control experiments confirm that NiOOH on the Ni–Co spinel oxide promotes the coadsorption of OH* and glycerol, which is crucial for the potential-dependent GOR mechanism.

In summary, we proposed a Fe substitution strategy to facilitate the formation of active NiOOH species in Ni–Co spinel oxide. *In situ*/*operando* analyses and control experiments confirm that foreign cation-promoted NiOOH formation improves properties regarding both the indirect and potential-dependent GOR mechanism, thereby enhancing the GOR performance for formate electrosynthesis.

This work was supported by the National Research Foundation of Korea (RS-2024-00343794 and RS-2024-00431568) funded by the Ministry of Science and ICT.

Data availability

The data supporting this article have been included as part of the ESI.†

Conflicts of interest

There are no conflicts to declare.

Notes and references

1 M. K. Goetz, M. T. Bender and K.-S. Choi, *Nat. Commun.*, 2022, **13**, 5848.
2 N. Han, Y. Wang, H. Yang, J. Deng, J. Wu, Y. Li and Y. Li, *Nat. Commun.*, 2018, **9**, 1320.
3 J. Eppinger and K.-W. Huang, *ACS Energy Lett.*, 2017, **2**, 188–195.
4 J. Ma, X. Wang, J. Song, Y. Tang, T. Sun, L. Liu, J. Wang, J. Wang and M. Yang, *Angew. Chem., Int. Ed.*, 2024, **63**, e202319153.
5 L. S. Oh, M. Park, Y. S. Park, Y. Kim, W. Yoon, J. Hwang, E. Lim, J. H. Park, S. M. Choi, M. H. Seo, W. B. Kim and H. J. Kim, *Adv. Mater.*, 2023, **35**, 2203285.
6 Q. Zhao, Z. Yan, C. Chen and J. Chen, *Chem. Rev.*, 2017, **117**, 10121–10211.
7 W. Chen, C. Xie, Y. Wang, Y. Zou, C.-L. Dong, Y.-C. Huang, Z. Xiao, Z. Wei, S. Du, C. Chen, B. Zhou, J. Ma and S. Wang, *Chemistry*, 2020, **6**, 2974–2993.
8 Y. Li, X. Lin and J. Du, *Inorg. Chem.*, 2021, **60**, 19373–19380.
9 V. Hadjiev, M. Iliev and I. Vergilov, *J. Phys. C: Solid State Phys.*, 1988, **21**, L199.
10 Z. Xiao, Y.-C. Huang, C.-L. Dong, C. Xie, Z. Liu, S. Du, W. Chen, D. Yan, L. Tao and Z. Shu, *J. Am. Chem. Soc.*, 2020, **142**, 12087–12095.
11 W. Gao, W. Gou, Y. Ma, R. Wei, J. C. Ho and Y. Qu, *ACS Appl. Energy Mater.*, 2019, **2**, 5769–5776.
12 R. T. M. van Limpt, M. Lao, M. N. Tsampas and M. Creatore, *Adv. Sci.*, 2024, **11**, 2405188.
13 C. Hu, Y. Hu, C. Fan, L. Yang, Y. Zhang, H. Li and W. Xie, *Angew. Chem., Int. Ed.*, 2021, **60**, 19774–19778.
14 M. T. Bender, Y. C. Lam, S. Hammes-Schiffer and K.-S. Choi, *J. Am. Chem. Soc.*, 2020, **142**, 21538–21547.
15 W. Chen, L. Xu, X. Zhu, Y. C. Huang, W. Zhou, D. Wang, Y. Zhou, S. Du, Q. Li and C. Xie, *Angew. Chem., Int. Ed.*, 2021, **60**, 7297–7307.
16 Y. Wang, Y.-Q. Zhu, Z. Xie, S.-M. Xu, M. Xu, Z. Li, L. Ma, R. Ge, H. Zhou, Z. Li, X. Kong, L. Zheng, J. Zhou and H. Duan, *ACS Catal.*, 2022, **12**, 12432–12443.

